Journal of Neuroscience Methods 244 (2015) 114–122

Contents lists available at ScienceDirect

Journal of Neuroscience Methods

journal homepage: www.elsevier.com/locate/jneumeth

Computational Neuroscience

Model validation of untethered, ultrasonic neural dust motes for cortical recording

Dongjin Seo[a,*], Jose M. Carmena[a,b], Jan M. Rabaey[a], Michel M. Maharbiz[a,1], Elad Alon[a,1]

[a] Department of Electrical Engineering and Computer Sciences, University of California, Berkeley, CA, USA
[b] Helen Wills Neuroscience Institute, University of California, Berkeley, CA, USA

HIGHLIGHTS

- We present neural dust: a method to power and communicate with sub-mm neural motes.
- We provide theory, modeling, and simulation of ultrasound-based neural dust.
- We provide experimental verification of the predicted scaling effects.
- We discuss using neural dust for central and peripheral nervous system recordings.

ARTICLE INFO

Article history:
Received 10 February 2014
Received in revised form 25 June 2014
Accepted 30 July 2014
Available online 7 August 2014

Keywords:
Ultrasonic energy harvesting
Backscatter communication
Chronic extra-cellular recording systems
Brain–machine interfaces

ABSTRACT

A major hurdle in brain–machine interfaces (BMI) is the lack of an implantable neural interface system that remains viable for a substantial fraction of the user's lifetime. Recently, sub-mm implantable, wireless electromagnetic (EM) neural interfaces have been demonstrated in an effort to extend system longevity. However, EM systems do not scale down in size well due to the severe inefficiency of coupling radio-waves at those scales within tissue. This paper explores fundamental system design trade-offs as well as size, power, and bandwidth scaling limits of neural recording systems built from low-power electronics coupled with ultrasonic power delivery and backscatter communication. Such systems will require two fundamental technology innovations: (1) 10–100 μm scale, free-floating, independent sensor nodes, or *neural dust*, that detect and report local extracellular electrophysiological data via ultrasonic backscattering and (2) a sub-cranial ultrasonic interrogator that establishes power and communication links with the neural dust. We provide experimental verification that the predicted scaling effects follow theory; $(127\ \mu m)^3$ neural dust motes immersed in water 3 cm from the interrogator couple with 0.002064% power transfer efficiency and 0.04246 ppm backscatter, resulting in a maximum received power of ~0.5 μW with ~1 nW of change in backscatter power with neural activity. The high efficiency of ultrasonic transmission can enable the scaling of the sensing nodes down to 10s of micrometer. We conclude with a brief discussion of the application of neural dust for both central and peripheral nervous system recordings, and perspectives on future research directions.

1. Introduction

Currently, the majority of neural recording is done through the direct electrical measurement of potential changes near relevant neurons during depolarization events called action potentials (AP). While the specifics vary across several prominent technologies, all of these interfaces share several characteristics: wired or wireless electrical connection between microelectrodes inside the brain to acquire useful neural signals and electronic circuits near the periphery to process them for brain–machine interfaces (BMI) (Biederman et al., 2013; Fan et al., 2011; Miranda et al., 2010; Szuts et al., 2011); a practical upper bound of several hundred implantable recording sites (Ganguly and Carmena, 2009; Harrison et al., 2007; Nicolelis et al., 2003; Stevenson and Kording, 2011); and the development of a biological response around the implanted electrodes which degrades recording performance over time (Chestek et al., 2011; Lind et al., 2013; Polikov et al., 2005; Prasad et al., 2012; Suner et al., 2005; Turner et al., 1999). To date, chronic clinical neural implants have proved to be successful in the short range (months to a few

* Corresponding author at: 490 Cory Hall, UC Berkeley, Berkeley, CA 94720, USA.
E-mail address: djseo@eecs.berkeley.edu (D. Seo).
[1] Joint senior authors.

http://dx.doi.org/10.1016/j.jneumeth.2014.07.025
0165-0270/

years) and for a small number of channels (10s–100s) (Alivisatos et al., 2013). A tetherless, high density, chronic interface to enable recording and stimulation from thousands of sites in a clinically relevant manner with little or no tissue response remains as one of the grand challenges of the 21st century.

The requirements for any computational platform employing microelectrodes to acquire useful neural signals are fairly stringent. The two primary constraints on the implanted device are size and power. On the one hand, implants placed into cortical tissue with scales larger than one or two cell diameters have well-documented tissue responses that are ultimately detrimental to performance. On the other hand, reducing the size of the implants reduces the distance between recording points, which decreases the absolute magnitude of the measured potentials. This decreased amplitude necessitates reductions in the noise from the electronics, which in turns requires higher power. This goes against the observation that smaller devices collect less power, and that building sufficiently low-power electronics becomes extremely challenging. Additionally, to eliminate the risk of infection associated with the transcutaneous/trans-cranial wires required for communication and power, such tethers should be avoided as much as possible; a wireless hub is therefore essential to relay the information recorded by the device through the skull.

Several energy modalities exist for powering and communicating with implants, and implantable wireless neural interfaces have recently been demonstrated in an effort to extend system longevity. The most popular existing wireless transcutaneous energy transfer technique relies on electromagnetics (EM) as the energy modality (Rabaey et al., 2011). An external transmitter generates and transfers information through purely electric (Sodagar and Amiri, 2009) or magnetic (Lee et al., 2010) near field or electromagnetic far field coupling (Yakovlev et al., 2012); this energy can be harvested by the implanted device and converted into a stable DC supply voltage. Energy transmission via magnetic near field has been used in a wide variety of medical applications and is the principal source of power for cochlear implants (Clark, 2003). As EM requires no moving parts or the need for chemical processing or temperature gradients, it is considered more robust and stable than other forms of energy scavenging. When used in-body, however, the power density of EM coupling is restricted by the potential adverse health effects associated with excess tissue heating in the human body due to electromagnetic fields. Ultimately, high attenuation in brain tissue and geometry-dependent magnetic coupling limit the transfer efficiency of electromagnetics, especially for miniature implants (Biederman et al., 2013].

Alternatively, acoustic waves can transmit energy between two piezoelectric transducers. Acoustic energy transmission has been used for various military applications, such as underwater (Istepanian and Stojanovic, 2002) and through-wall communication (Hu et al., 2003). Unlike electromagnetics, using ultrasound as an energy transmission modality never entered into widespread consumer application, and was often overlooked because the efficiency of electromagnetics for short distances and large apertures is superior. However, for the scales discussed here and in tissue (i.e., aqueous media), the fact that acoustic waves travel at much lower velocity allows operation at dramatically lower frequencies, and more importantly, the acoustic loss in tissue is generally substantially smaller than the equivalent attenuation of electromagnetics. This is also manifested by the stark difference in the time-averaged acceptable intensity for ultrasound for cephalic applications, as regulated by the FDA, which is approximately 9× (94 mW/cm^2) for general-purpose devices and 72× (720 mW/cm^2) for devices conforming to output display standards (ODSs) compared to EM which is limited to 10 mW/cm^2 (FDA, 2008).

In this paper, we present a neural recording platform built from low-power electronics coupled with ultrasonic power delivery and backscatter communication. In particular, we propose an ultra-miniature and extremely compliant system (Fig. 1) that enables significant scaling in the number of neural recordings from the brain while providing a path toward truly chronic BMI. This is achieved via two fundamental technology innovations: (1) 10–100 μm scale, free-floating, independent sensor nodes, or *neural dust*, that detect and report local extracellular electrophysiological data, and (2) a *sub-cranial interrogator* that establishes power and communication links with the neural dust. The interrogator would be placed beneath the skull (to avoid strong attenuation of ultrasound by bone), possibly even below the dura mater, and would be powered by an external transceiver via EM power transfer. The theoretical treatment presented in this paper builds on an earlier published pre-print; that work also contains a detailed analysis detailing why EM coupling is not scalable for sub-mm cortical recordings (Seo et al., 2013).

2. Model and theory

2.1. Piezoelectric materials

Piezoelectricity refers to the phenomenon present in certain solid (usually crystalline) materials where there is an interaction between the mechanical and electrical states. As a result, piezoelectric materials can transduce electrical energy into mechanical energy and vice versa by changing lattice structure, and this state change is accessible via either electrical stimulation or mechanical deformation. These materials serve as a critical component in the construction of probes that generate ultrasonic waves to enable ultrasound technology used in the medical industry. A relatively wide range of piezoelectric materials are available, each suitable for different applications. For instance, piezoelectric polymer compounds such as PVDF are primarily used to construct broadband, high-sensitive hydrophones due to their low quality factor and high piezoelectric voltage constant. On the other hand, a ceramic compound known as lead zirconate titanate (PZT) is a popular choice for high performance diagnostic ultrasonic imaging due to its greater sensitivity, higher operational temperature, and exceptional electromechanical coupling coefficient (k). The electromechanical coupling coefficient is a figure of merit used to describe the ability of a material to convert one form of energy into another, and PZT's high k value makes it an attractive material. When used in-body, however, the lead content of PZT makes it difficult to introduce into human tissue in chronic applications. A number of alternative, implantable piezoelectric materials, such as barium titanate ($BaTiO_3$), aluminum nitride (AlN) and zinc oxide (ZnO) (Przybyla et al., 2011), exist with material properties slightly inferior to PZT. Experiments presented in this paper were carried out with PZT due to the relative ease of obtaining PZT crystals with varying geometry. The PZT was fully encapsulated in PDMS silicone; its effects are discussed in Section 4.

2.2. Transducer model

Due to the importance of piezoelectric transducers in various applications, a number of models of the electromechanical operation of one-dimensional piezoelectric and acoustic phenomena have evolved over the years. The KLM model is arguably the most common equivalent circuit, and is a useful starting point to construct a full link model with the intent of examining scaling and system constraints (Krimholtz et al., 1970). The basic model includes a piezoelectric transducer with electrodes fully covering the two largest faces of the transducer. The entire transducer is modeled as a frequency-dependent three-port network, consisting of one electrical port (where electric power is applied or

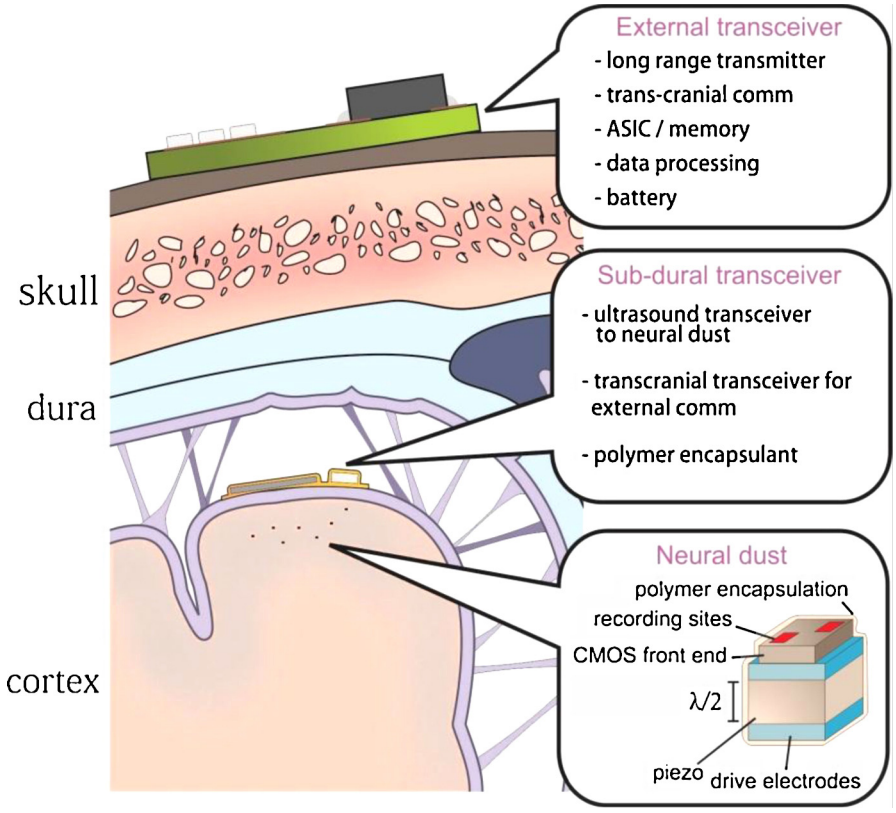

Fig. 1. Neural dust system diagram showing the placement of ultrasonic interrogator under the skull and the independent neural dust sensing motes dispersed throughout the brain.

collected) and two acoustical ports (where mechanical waves are produced or sensed from the front and back faces of the transducer). The parallel-plate capacitance due to the electrodes and the frequency-dependent acoustic capacitance are modeled as C and X_i, respectively, and the transduction between electrical and mechanical domains is modeled as an ideal electromechanical transformer with a turn ratio of φ connected to the middle of a transmission line of length $\lambda/2$, as shown in Fig. 2. Assuming an infinite 2D plate piezoelectric transducer of thickness h, the resonant frequency is set by $h = \lambda/2$; at the resonant frequency, the ultrasound wave impinging on either the front or back face of the transducer will undergo a 180° phase shift to reach the other side, causing the largest displacement between the two faces. This observation implies that phase inversion only exists at the odd harmonics of the fundamental mode in a given geometry.

The KLM model, however, was derived under the assumption of pure one-dimensional thickness vibration, and therefore can only provide a valid representation for a piezoelectric transducer with an aspect ratio (width/thickness) greater than 10; such a transducer would mainly resonate in the thickness mode (Roa-Prada et al., 2013). Given the extreme miniaturization target for neural dust, a cube dimension (aspect ratio of 1:1:1) is a better approximation of the geometry than a plate (aspect ratio > 10:10:1). Due to Poisson's ratio and the associated mode coupling between resonant modes along each of the three axes of the cube, changing aspect ratio alters the resonant frequencies (Holland, 1968). The effect of resonance shift is included in the KLM model by extracting the effective acoustic impedance of the neural dust from a model simulated using a 3D finite element package, COMSOL Multiphysics (COMSOL, Stockholm, Sweden). The piezoelectric transducers for both the planar interrogator (i.e., 2D) and the neural dust must be designed to resonate at the same frequency to maximize the link efficiency. Therefore, the interrogator thickness is varied to match the fundamental thickness mode of the neural dust.

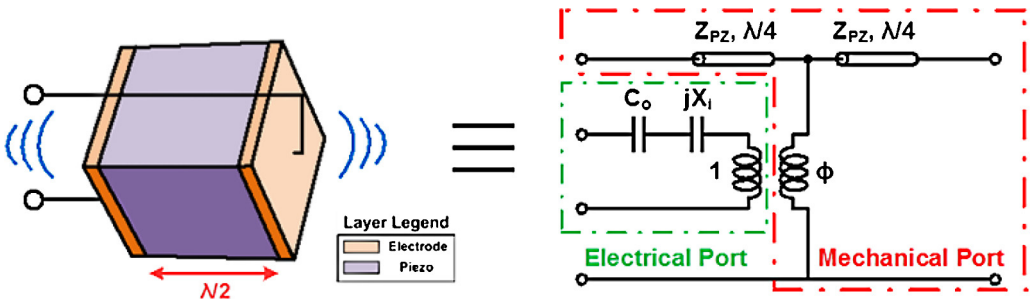

Fig. 2. KLM model of a dust mote's piezoelectric transducer, showing one electrical port and two mechanical ports. Coupling between the domains is modeled with an ideal electromechanical transformer.

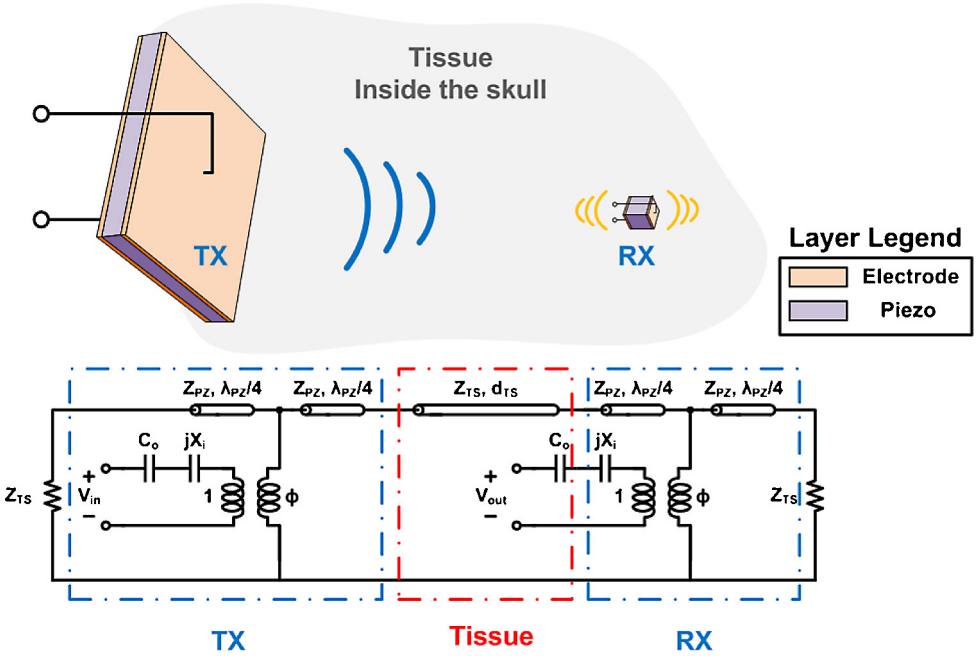

Fig. 3. Complete single interrogator, single neural dust power and communication through link models.

Lastly, we can calculate the mechanical quality factor Q (see Section 4):

$$Q = \frac{f_a^2}{2\pi f_r Z_r C_p (f_a^2 - f_r^2)}$$

where f_a and f_r represent anti-resonant (where impedance is maximized) and resonant frequencies (where impedance is minimized), respectively; Z_r represents the impedance at resonance, and C_p is the low-frequency capacitance.

2.3. Mote placement

As the pressure field generated by a uniform continuous-wave excited piezoelectric transducer propagates through the tissue medium, the characteristics of the pressure field change with distance from the source. The varying field is typically divided into two segments, *near field* and *far field*. In the near field, the shape of the pressure field is cylindrical and the envelope of the field oscillates. At some point distal to the transducer, however, the beam begins to diverge and the pressure field becomes a spherically spreading wave, which decays inversely with distance. The transition between the near and far field is where the pressure field converges to a natural focus, and the distance at which this occurs is called the Rayleigh distance, defined as,

$$L = \frac{D^2 - \lambda^2}{4\lambda} \approx \frac{D^2}{4\lambda}, D^2 \gg \lambda^2$$

where D is the aperture of the transmitter and λ is the wavelength of ultrasound in the propagation medium (Kino, 1987). In order to maximize the received power, it is preferable to place the receiver at one Rayleigh distance where the beam spreading is at a minimum.

2.4. Power delivery simulation methods

The complete link model, shown in Fig. 3, is implemented in MATLAB (Mathworks, Natick, MA) with the limitations of the KLM model (as outlined in the previous section) corrected via COMSOL simulations. The model is divided into three parts: (1) the ultrasonic interrogator or *transmitter*, (2) tissue, and (3) the neural dust or *receiver*. A signal generator and amplifying stages produce power for the ultrasonic interrogator and the ultrasonic wave launched by the transmitter penetrates brain tissue, modeled as a lossy transmission line, and a fraction of that energy is harvested by the ultrasonic receiver, or neural dust.

To compute the link power transfer efficiency, the model can be decomposed into a set of linear and time-invariant two-port parameters, representing a linear relationship between the input and output voltage. Here, we choose to represent the input-to-output relationship using ABCD parameters (Pozar, 2011), which simplifies analysis of cascades of two-port networks through simple matrix multiplication. By representing the link model as a two-port network, we can come to conclusions concerning optimal power transfer efficiency (or "gain").

2.5. Backscattering communication

For the ultra-miniature, chronic implants discussed here (which have stringent requirements on both the size and power), broadcasting neural recording data from the dust motes to the interrogator by building a fully active transmitter onto the tiny motes is infeasible. Therefore, we adopt a communication method called *backscattering*, used in radio frequency identification (RFID) technologies (Finkenzeller, 2010). In RFID, passive (i.e., batteryless) tags (like the common keycard that opens doors) receive RF energy from a nearby interrogator and re-radiate this energy; while doing so, the tags can modulate the re-radiated energy and thus encode information. Modulation of the backscattered RF energy can be achieved by varying the load impedance, which changes the coefficient of reflectivity. Backscattering receivers do not need batteries or significant capacitive energy storage, thus extending lifetimes, eliminating the risk of battery leakage, and removing the significant impediment to size scaling imposed by large capacitors. Importantly, the many communication strategies developed for electromagnetic backscattering can be applied to any link, regardless of the transmission channel modality (i.e., in our case, ultrasound).

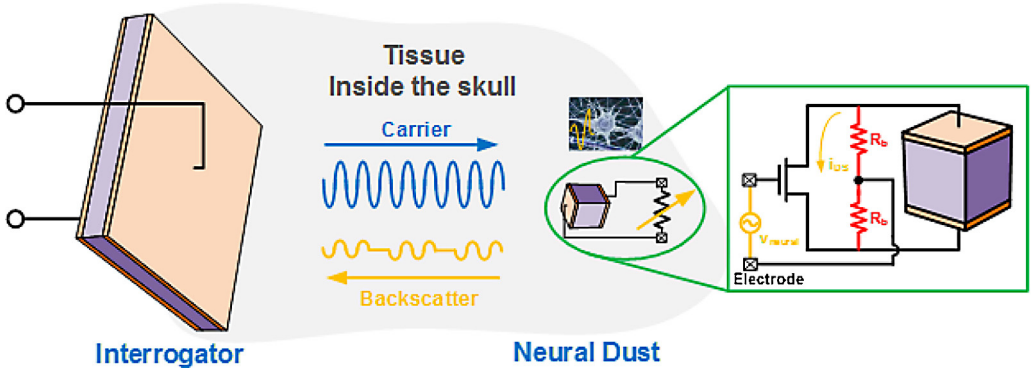

Fig. 4. A field effect transistor or FET (right) varies the electrical load impedance as a function of potential between two electrodes placed in the extracellular fluid; this modulates the ultrasonic wave reflectivity of the dust thereby modifying the backscattered wave.

2.6. Communication system architecture

Ideally, the simplest neural dust mote would consist of a piezoelectric transducer with a set of surface electrodes that can record the occurrence of a neural spike. The extracted measurement would be reported back to the interrogator if the information can somehow be encoded on the reflected ultrasound wave via modulation.

We propose a method outlined in Fig. 4, where the drain (D) and source (S) of a single field-effect transistor (FET) sensor are connected to the two terminals of a piezoelectric transducer while the FET modulates the current I_{DS} as a function of a gate (G) to source voltage, V_{GS}. The resistors R_b act to cause the neural potential to appear between the gate and both of the D/S terminals of the transistors while superimposing the AC waveform from the ultrasonic transducer across these same two terminals. In this manner, even though the electrical D/S terminals swap every half cycle, the V_{GS} of the FET is modulated by the neural signal during both halves of the cycle.

The circuit achieves this superposition by relying on the fact that the neural signals occupy a much lower frequency band than the ultrasound, and that the ultrasound transducer itself has a capacitive output impedance (C_{piezo}). Thus, R_b should be chosen so that $1/(R_b \times C_{piezo})$ is placed well above the bandwidth of V_{neural} (>10 kHz) (Nicolelis et al., 2003) but well below the ultrasound frequency (i.e., 10 MHz for a 100 μm node).

Since modulation of I_{DS} in turn modulates the impedance seen across the two piezoelectric drive terminals, the FET effectively modulates the backscattered signal seen by a distant transmitter. The change in the nominal level of I_{DS} is a function of V_{GS}, which can be up to 10 μV (V_{neural}) for a 100 μm dust node near an active neuron (Du et al., 2011). The sensitivity, S, to the action potential (AP), then, is defined as the change in I_{DS} with respect to V_{GS} normalized by the nominal I_{DS} (in addition to the current through R_b) and V_{neural},

$$S = \frac{V_{neural}}{I_{DS} + (V_{DS}/2R_b)} \frac{\partial I_{DS}}{\partial V_{GS}} = V_{neural} \frac{g_m}{I_{DS} + (V_{DS}/2R_b)}$$

Since g_m (the transconductance of an FET) is directly proportional to I_{DS}, in order to maximize g_m/I_{DS} (i.e., achieve the largest g_m for a given I_{DS}), we would like to operate the FET in its steepest region – specifically, deep sub-threshold where it looks like a bipolar junction transistor (BJT). Therefore, the nominal V_{GS} bias can be 0 V, which simplifies the bias circuitry. The modulation of the current is equivalent to a change in effective impedance of the FET, or the electrical load to the piezoelectric transducer. This variation in the load impedance affects the ultrasonic wave reflectivity at the neural dust and modifies the wave that is backscattered. Note that in order to maximize the sensitivity (i.e., operating the transistor in deep sub-threshold), the system should be constrained such that the piezoelectric voltage is never too large compared to the threshold voltage.

2.7. Backscattering simulation methods

From the complete link model shown in Fig. 3, we note that the change in the electrical impedance of the FET load induces a change in the input admittance (or the input power) of the two-port network. The interrogator (receiver) must be able to detect this change in the input power level in order to resolve the occurrence of a neural spike. The model is implemented in MATLAB and the change in the input power level of the two-port network is computed as,

$$\Delta P_{in} \propto \left| \frac{Y_{in,spike} - Y_{in,nom}}{Y_{in,nom}} \right|$$

where $Y_{in,spike}$ and $Y_{in,nom}$ denote input admittance of the two-port network with and without a neural spike, respectively. The FET sensor design methodology and trade-offs are detailed in an earlier published pre-print (Seo et al., 2013). That work also concludes that the mote scaling is ultimately limited by the achievable differential signals between the electrodes and motivate the need to break this inherent interplay between the size of the individual implants and the achievable signal-to-noise ratio (SNR).

Since the tradeoff does not directly derive from the neural dust dimension, but from electrode separation, one approach may be to add very small footprint (~1–5 μm wide) "tails" which position a single (or multiple) electrode relatively far (>100 μm) from the base of the neural dust implant. This would result in the design shown in Fig. 5, where instead of placing a single differential surface electrode on neural dust, the neural dust can consist of a short strand

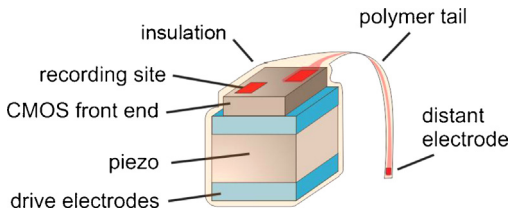

Fig. 5. Neural dust mote with an ultra-compliant flexible polyimide "tail". The entire mote, not including the electrodes (red squares), is coated with a polymer or ceramic insulating thin film. Note the one recording electrode (red square, left). The reference electrode can either be on-mote (red square, right) or shorted to a conductive thin film to a distant electrode (increasing the separation between the recoding site and reference electrode). The "tail" increases inter-electrode distance and thus the magnitude of the voltage seen across electrodes when recording extracellularly. (For interpretation of the references to color in this figure legend, the reader is referred to the web version of this article.)

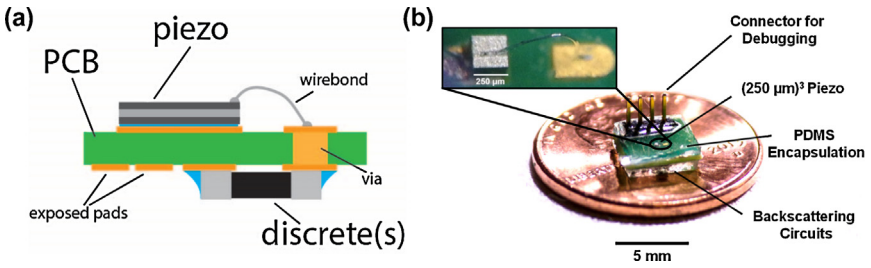

Fig. 6. (a) Assembly prototype schematic (b) a picture of the complete prototype with a white light micrograph of PZT crystal mounted on board.

of flexible and ultra-compliant substrate populated with recording sites. Due to increased inter-electrode distance, the tail electrode increases the achievable SNR; simulations indicate that the addition of the tail electrode can enable further scaling of the neural dust mote with only a minor adjustment to the original design (Seo et al., 2013).

3. Materials and methods

3.1. Sample preparation

The assembly prototype, shown in Fig. 6, was realized on a 31 mil thick two-layer FR-4 board where metalized PZT coupons of various thicknesses (PSI-5A4E, Piezo Systems, Woburn, MA and PZT 841, APC Internationals, Mackeyville, PA) were bonded to pre-soldered bumped electrodes on one side of the board using solder paste. The FET (RV1C002UN, Rohm Semiconductor, Kyoto, Japan) and bias resistors for ultrasonic communication were assembled onto the side opposite to where the PZTs were mounted prior to bonding. The PZTs were then wafer saw diced, with non-bonded areas dropping off and leaving an array of small PZT crystals bonded to the PCB. Next, a single wirebond made the connection between the top plate of the PZT and an electrode on the PCB, completing the circuit. Finally, the entire assembly was coated in PDMS (Sylgard 184, Dow Corning, Midland, MI) to protect the wirebond and provide insulation. The pitch between the unit cells is limited by the size of the discrete components and is roughly 2.3 mm × 2 mm.

3.2. Electrical characterization

Electrical properties of the PZT crystals on the assembled prototype were measured using a vector network analyzer (VNA) (E5071C ENA, Agilent Technologies, Santa Clara, CA). The device under test (DUT) was de-embedded using an open/short/load scheme in order to remove the board and fixture parasitics and calibrate out the cable loss. The open/short/load structures were fabricated on the same board.

3.3. Ultrasonic characterization

Ultrasonic power transfer and communication were performed using a home-built setup shown in Fig. 7. A 5 MHz or 10 MHz single

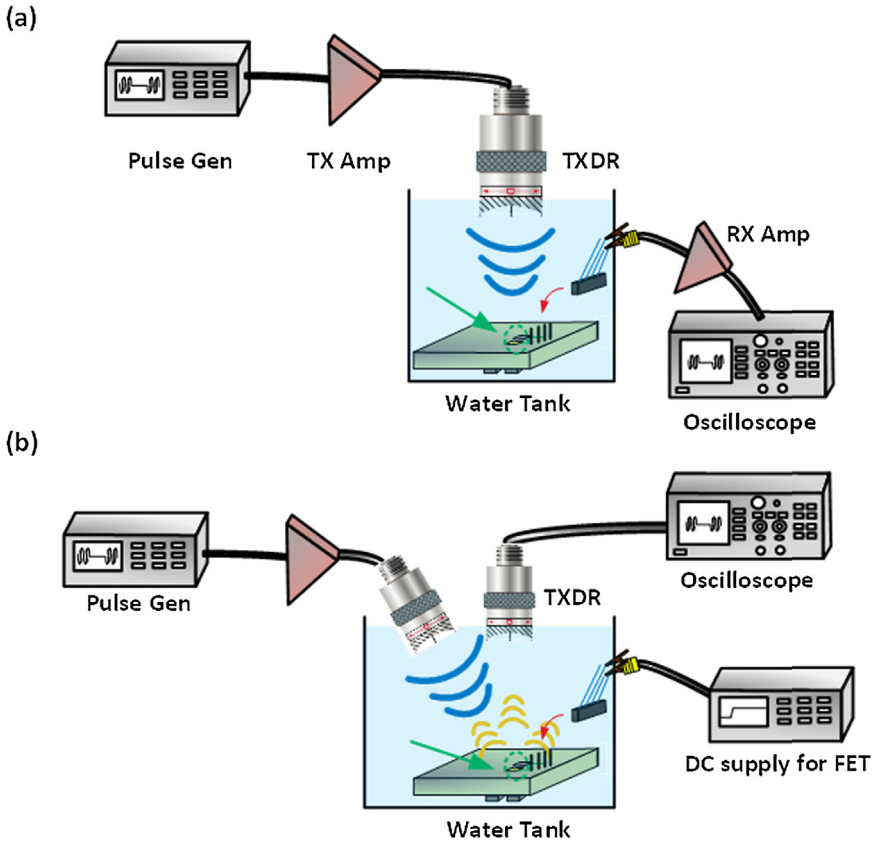

Fig. 7. Acoustic characterization setup with a calibrated ultrasonic transducer for (a) power delivery and (b) backscatter communication verification.

element transducer (6.3 and 6.3 mm active areas, respectively; ~30 mm focal distance; Olympus, Waltham, MA) was mounted on a computer-controlled 2D translating stage (VelMex, Bloomfield, NY). The transducer's output was calibrated using a hydrophone (HGL-0400, Onda, Sunnyvale, CA). Assembly prototypes were placed in a water container such that transducers could be immersed in the water at a distance of approximately 3 cm directly above the prototypes. A programmable pulse generator (33522B, Agilent Technologies, Santa Clara, CA) and radio frequency amplifier (A150, ENI, Rochester, NY) were used to drive transducers at specified frequencies with sinusoidal pulse trains of 10-cycles and a pulse-repetition frequency (PRF) of 1 kHz. The received signals were amplified with a radio frequency amplifier (BT00500-AlphaS-CW, Tomco, Stepney, Australia), connected to an oscilloscope (TDS3014B, Tektronix, Beaverton, OR) to collect ultrasound signals and record them using MATLAB (Mathworks, Natick, MA). For communication measurements, in order to eliminate feedthrough between transmit and receive stages and reflections from the board, separate transmit and receive transducers were used.

4. Results

The total integrated acoustic output power of the transducer at various frequencies over the 6 dB bandwidth of the beam was measured using a calibrated hydrophone. Nominally, spatial-peak temporal-average I_{SPTA} was kept at 29.2 μW/cm^2, resulting in a total output power of ~1 μW at the focal point, with a peak rarefaction pressure of 25 kPa and a mechanical index (MI) of 0.005. Both the de-rated I_{SPTA} and MI were far below the FDA regulation limit of 720 mW/cm^2 and 1.9, respectively (FDA, 2008).

4.1. Measured power transfer scaling matches simulation

Fig. 8(a) shows the measured power delivery efficiency of the fully assembled prototype with cable loss calibrated out for various mote sizes as compared to analytical predictions made for this same setup. Measured results matched the simulated model behavior very closely across all mote sizes, with the exception of a few smaller mote dimensions, likely due to the sensitivity to transducer position and the ultrasound beamwidth. The measured efficiency of the link for the smallest PZT crystal (127 μm)^3 was 2.064×10^{-5}, which resulted in 20.64 pW received at the dust node nominally. A maximum of 0.51 μW can be recovered at the dust node if the transmit output power density was kept at 720 mW/cm^2. Such low power level harvested by the PZT is mainly due to the extreme inefficiency of broadband transducers that were used for the experiments; our model predicts that dedicated, custom-made transducers at each mote dimension with optimal focal point and electrical input impedance matching could result in more than 2 orders of magnitude improvement in the harvested power level (Seo et al., 2013).

4.2. Mechanical dampening of resonance does not play a large role in power transfer efficiency

In order to further validate the model framework, we measured both the frequency response of harvested power on the PZT and the impedance spectroscopy of PZT at each mote dimension. Fig. 8(b) shows a representative impedance plot of a (250 μm)^3 PZT crystal compared to simulation. We note that the mechanical loading of the circuit board itself (FR-4), the PDMS, and water heavily dampened the electro-mechanical resonances as compared to the unloaded condition (air backing); this decreased the mechanical quality factor (Q) of the PZT crystal from ~110 to ~5.

The frequency response of electrical voltage harvested on a (250 μm)^3 PZT crystal is shown in Fig. 8(c). We measured the resonant frequency to be at 6.1 MHz, which matches the shift in the resonant frequency predicted for a cube due to Poisson's ratio and the associated mode coupling between resonant modes along each of the three axes of the cube, as discussed previously. Furthermore,

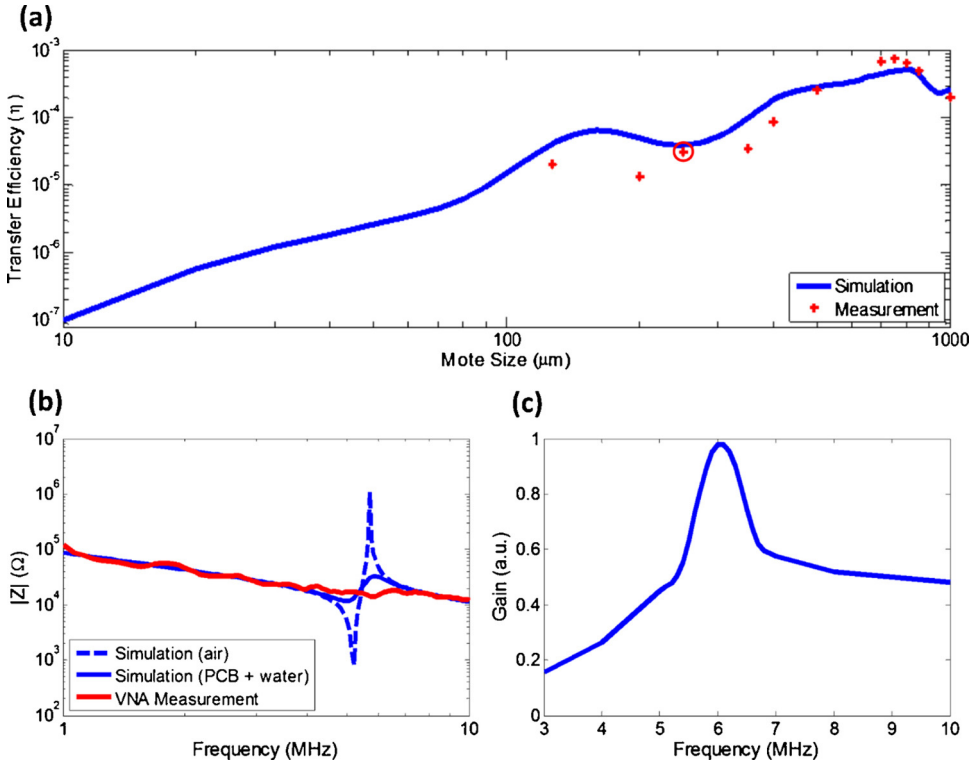

Fig. 8. (a) Measured power transfer efficiency at various mote sizes matches simulated behavior closely. For each mote dimension, both (b) the impedance spectroscopy and (c) frequency response of harvested power on the PZT reinforces the reliability of the simulation framework.

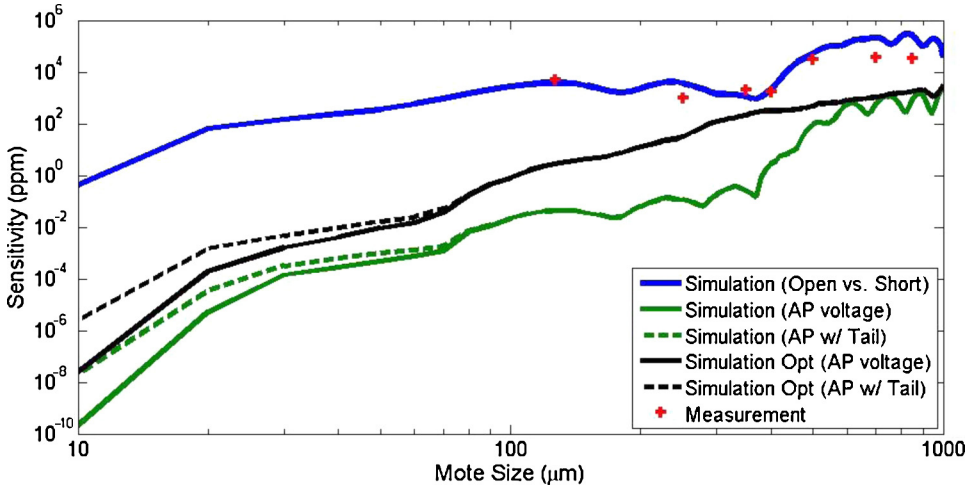

Fig. 9. Simulated and measured backscatter sensitivity scaling plot for various impedance levels.

the calculated Q of 4.8 matched the electrically measured Q of the PZT. Despite the drastic reduction in the mechanical Q of the PZT crystals, simulations show that the backscattered signal level only decreased by roughly ~19% (between the mechanically unloaded and loaded conditions).

4.3. Measured backscatter signal levels for dust motes match simulation

The backscatter simulation framework was verified by measuring the difference in the backscattered voltage level and computing the ppm change (i.e., sensitivity) when the PZT crystal was electrically open versus shorted. For this experiment, a single broadband transducer was used to both transmit and receive reflected signal and its network model was estimated based on the VNA measurements. Backscatter measurement results, as shown in Fig. 9, matched the analytical model behavior very closely and the sensitivity of $(127\ \mu m)^3$ dust mote was ~5000 ppm. The measurement of backscatter sensitivity is currently limited by heat-induced drift noise of the instruments and the inaccurate model of the broadband transducer. This also implies that we were unable to detect much lower backscatter signals generated on $(127\ \mu m)^3$ dust mote when a more realistic action potential voltage appeared at the V_{GS} of the FET to modulate the impedance by less than 0.1%, as shown in Fig. 9. Using this measurement, however, we were able to verify our backscatter simulation framework. A properly tuned system which accounts for temperature changes in the instruments can significantly improve the measured sensitivity. Also note that the simulation predicts that under a low-drift setup, where a dedicated, custom-made transducer achieves optimal focal distance and electrical input impedance at each mote dimension, the achievable backscatter sensitivity will substantially increase the backscatter sensitivity with an action potential voltage at the input of the FET, as shown in Fig. 9.

5. Discussion

The experimental results indicate that the analytical model for power coupling to very small piezoelectric nodes using ultrasound is accurate down to, at least, ~100 μm scales and likely lower. We also demonstrate that our model can correctly capture the effects of changing the load impedance of a piezocrystal on the backscatter signals at such scales. It remains to be seen just how small a node can be fabricated before loss of function; Seo et al. (2013) discusses the likely scaling limits (set by physics, physiology and semiconductor manufacturing constraints) in more detail.

Note that measurements of even smaller motes (<127 μm) were limited not by the prototype assembly process, but by commercial availability of PZT substrates. Moving forward, we are harnessing the considerable volume of research and techniques that has gone into micro- and nanoelectromechanical RF resonators (Lin et al., 2005; Sadek et al., 2010) and thin-film piezoelectric transducers (Przybyla et al., 2011; Trolier-McKinstry and Muralt, 2004) to facilitate extremely small (10s of μm) dust motes and to truly assess the scaling theory.

While the work here pre-supposes a system for recording from the central nervous system (more specifically, the neocortex), neural dust may also find utility in peripheral nervous system applications as well. Systems that can record stably in mammals from within the epineurium remain an open challenge. Neural dust approaches seem eminently suited for this task as dust motes could be introduced micro-surgically and then interrogated externally in a manner analogous to the cortical recording approach assumed in this paper. This would obviate the need for trans-epineurial wires and/or access points and provide recording sites which are much smaller than that possible with RF communication (again, as pointed out in this paper and analyzed in Seo et al., 2013).

Lastly, these results point to several technology challenges. The integration of extremely small piezoelectric transducers with integrated electronics in a properly encapsulated package, such as an inert polymer or insulator film (a variety of such coatings are used routinely in neural recording devices; these include parylene, polyimide, silicon nitride and silicon dioxide, among others) while exposing two electrodes to the brain for extracellular recording remains an open question.

In addition, building a complete system will require the design and implementation of suitably sensitive sub-cranial transceivers which can operate at low power. A number of highly sensitive RF wireless receivers with <1 mW of DC power consumption (and, thus, heat generated) have been demonstrated (e.g., Otis et al., 2005). In addition, the sensitivity requirements of an interrogator in a physiological system are more stringent than predicted due to additional interferences (e.g., ultrasonic wave reflections arising from local density variations, micro-motion, micro-vasculature, etc.). Such reflections will likely lead to inter-symbol interference; filtering and/or adaptive algorithms (Proakis, 2000) can be applied to track these sufficiently slow variations and reverse the effects of reflections. Alternatively, one could potentially utilize a pulse-based system to uniquely discriminate the various reflections based on their arrival times.

The sub-cranial transceiver design also introduces multi-interrogator, multi-dust communication possibilities which make

use of modern communication techniques such as beam steering and multi-input, multi-output (MIMO) system theory. When employing multiple embedded dust motes, interrogating and identifying the signal from an individual neural dust mote is challenging due to interferences from surrounding motes. This necessitates an interrogator with multiple, independently addressable transducer elements acting in an array; optimization at both algorithm and hardware implementation levels must be fully explored to achieve sufficient interference suppression to resolve simultaneous signals from different motes via spatial or time multiplexing. Furthermore, neural dust motes with aspect ratios close to 1:1:1 will not only couple energy into modes along the two axes perpendicular to the transmission axis, they will also re-radiate along those axes. This means motes lying near each other on a horizontal plane (relative to the top surface of the cortex) may see inter-mote signal mixing, making them amenable to multi-mote ad-hoc type communication networks and reduce its sensitivity to mis-orientation of dust motes.

Acknowledgements

The authors thank Dr. Patrick Goodwill, Dr. Paul Lum, Daniel Hensley (UC Berkeley), and Prof. Mikhail G. Shapiro (Caltech) for ultrasound equipment and test setup advice, Filip Maksimovic (UC Berkeley) for help with hydrophone measurements, and Dr. Peter Ledochowitsch (Allen Institute) and Dr. Alexander Bertrand (KU Leuven) for valuable discussions. This work was supported by a Graduate Fellowship from the National Science Foundation to DS and the Bakar Fellowship for JMC and MMM.

References

Alivisatos AP, Chun M, Church GM, Deisseroth K, Donoghue JP, Greenspan RJ, et al. The brain activity map. Science 2013;339:1284–5.

Biederman W, Yeager DJ, Narevsky N, Koralek AC, Carmena JM, Alon E, et al. A fully-integrated, miniaturized (0.125 mm^2) 10.5 μW wireless neural sensor. IEEE J Solid-State Circuits 2013;48(4):960–70.

Chestek CA, Gilja V, Nuyujukian P, Foster JD, Fan JM, Kaufman MT, et al. Long-term stability of neural prosthetic control signals from silicon cortical arrays in rhesus macaque motor cortex. J Neural Eng 2011;8:1–11.

Clark GM. Cochlear implants: fundamentals and applications. New York: Springer-Verlag; 2003.

Du J, Blanche TJ, Harrison RR, Lester HA, Masmanidis SC. Multiplexed, high density electrophysiology with nanofabricated neural probes. PLoS ONE 2011;6(10):1–11.

Fan D, Rich D, Holtzman T, Ruther P, Dalley JW, Lopez A, et al. A wireless multi-channel recording system for freely behaving mice and rats. PLoS ONE 2011;6(7):1–9.

FDA. Information for manufacturers seeking marketing clearance of diagnostic ultrasound systems and transducers; 2008.

Finkenzeller K. RFID handbook: fundamentals and applications in contactless smart cards, radio frequency identification and near-field communication. Chichester, UK: John Wiley & Sons; 2010.

Ganguly K, Carmena JM. Emergence of a stable cortical map for neuroprosthetic control. PLoS Biol 2009;7(7):113.

Harrison RR, Watkins PT, Kier RJ, Lovejoy RO, Black DJ, Greger B, et al. A low-power integrated circuit for a wireless 100-electrode neural recording system. IEEE J Solid-State Circuits 2007;42(1):123–33.

Holland R. Resonant properties of piezoelectric ceramic rectangular parallelepipeds? J Acoust Soc Am 1968;43(5):988–97.

Hu Y, Zhang X, Yang J, Jiang Q. Transmitting electric energy through a metal wall by acoustic waves using piezoelectric transducers. IEEE Trans UFFC 2003;50(7):773–81.

Istepanian RSH, Stojanovic M. Underwater acoustic signal processing and telemetry systems, theory and applications. Kluwer Academic Publishers; 2002.

Kino GS. Acoustic waves: devices, imaging, and analog signal processing. Englewood Cliffs, NJ: Prentice Hall; 1987.

Krimholtz R, Leedom DA, Matthaei GA. New equivalent circuits for elementary piezoelectric transducers. Electron Lett 1970;6(13):398–9.

Lee SB, Lee H, Kiani M, Jow U, Ghovanloo M. An inductively powered scalable 32-channel wireless neural recording system-on-a-chip for neuroscience applications. IEEE Trans BioCAS 2010;4(6):360–71.

Lin Y, Li S, Ren Z, Nguyen CTC. Low phase noise array-composite micromechanical wine-glass disk oscillator. IEEE Electron Devices Meet 2005:1–4.

Lind G, Linsmeier CE, Schouenborg J. The density difference between tissue and neural probes is a key factor for glial scarring. Sci Rep 2013., http://dx.doi.org/10.1038/srep02942, Scientific Reports 3, Article number: 2942.

Miranda H, Gilja V, Chestek CA, Shenoy KV, Meng TH. HermesD: a high-rate long-range wireless transmission system for simultaneous multichannel neural recording applications. IEEE Trans BioCAS 2010;4(3):181–91.

Nicolelis MAL, Dimitrov D, Carmena JM, Crist R, Lehew G, Kralik JD, et al. Chronic, multisite, multielectrode recordings in macaque monkeys. Proc Natl Acad Sci 2003;100:11041–6.

Otis B, Chee YH, Rabaey JM. A 400 μW-RX, 1.6 mW-TX super-regenerative transceiver for wireless sensor networks. IEEE ISSCC 2005;1:396–7.

Polikov VS, Tresco PA, Reichert WM. Response of brain tissue to chronically implanted neural electrodes. J Neurosci Methods 2005;148:1–18.

Pozar DM. Microwave engineering. New York, NY: John Wiley & Sons; 2011.

Prasad A, Xue QS, Sankar V, Nishida T, Shaw G, Streit W, et al. Comprehensive characterization and failure modes of tungsten microwire arrays in chronic neural implants. J Neural Eng 2012;9:1–21.

Proakis JG. Digital communication. New York, NY: McGraw-Hill; 2000.

Przybyla RJ, Shelton SE, Guedes A, Izyumin II, Kline MH, Horsley DA, et al. In-air rangefinding with an ALN piezoelectric micromachined ultrasound transducer. IEEE Sens J 2011;11(11):2690–7.

Rabaey JM, Mark M, Chen D, Sutardja C, Tang C, Gowda S, et al. Powering and communicating with mm-size implants. IEEE DATE Conf 2011:1–6.

Roa-Prada S, Scarton HA, Saulnier GJ, Shoudy DA, Ashdown JD, Das PK, et al. An ultrasonic through-wall communication (UTWC) system model. J Vib Acoust 2013;135(1):1–12.

Sadek AS, Karabalin RB, Du J, Roukes ML, Koch C, Masmanidis SC. Wiring nanoscale biosensors with piezoelectric nanomechanical resonators. Nano Lett 2010;10:1769–73.

Seo D, Carmena JM, Rabaey JM, Alon E, Maharbiz MM. Neural dust: an ultrasonic, low power solution for chronic brain–machine interfaces; 2013 arXiv:1307.2196.

Sodagar AM, Amiri P. Capacitive coupling for power and data telemetry to implantable biomedical microsystems. IEEE EMBS Conf 2009:411–4.

Stevenson I, Kording K. How advances in neural recording affect data analysis. Nat Neurosci 2011;14(2):139–42.

Suner S, Fellows MR, Vargas-Irwin C, Nakata GK, Donoghue JP. Reliability of signals from a chronically implanted, silicon-based electrode array in non-human primate primary motor cortex. IEEE Trans Neural SRE 2005;13(4):524–41.

Szuts TA, Fadeyev V, Kachiguine S, Sher A, Grivich MV, Agrochao M, et al. A wireless multi-channel neural amplifier for freely moving animals. Nat Neurosci 2011;14(2):263–9.

Turner JN, Shain W, Szarowski DH, Andersen M, Martins S, Isaacson M, et al. Cerebral astrocyte response to micromachined silicon implants. Exp Neurol 1999;156:33–49.

Trolier-McKinstry S, Muralt P. Thin film piezoelectrics for MEMS. J Electroceram 2004;12:7–17.

Yakovlev A, Kim S, Poon A. Implantable biomedical devices: wireless powering and communication. IEEE Commun Mag 2012;50(4):152–9.